Journal of
Materials Chemistry A

ROYAL SOCIETY
OF CHEMISTRY

PAPER

View Article Online
View Journal | View Issue

Check for updates

Cite this: *J. Mater. Chem. A*, 2025, **13**, 28546

Composite membranes with tailored interfaces for high-efficiency anion exchange membrane-based alkaline water and simulated alkaline seawater electrolysis

Yuhui Gong,[a] Yuanman Ni,[a] Tian Lan,[a] Han Song,[a] Hao Zhang,[a] Shujuan Wang,[a] Miaomiao Liu,[a] Tongshuai Wang,*[ab] Jian-Qiang Wang *[ab] and Linjuan Zhang *[ab]

Received 3rd July 2025
Accepted 28th July 2025

DOI: 10.1039/d5ta05372b

rsc.li/materials-a

Hydrogen production *via* water electrolysis is considered a cornerstone technology for building a sustainable and carbon-free energy system. However, current electrolysis technologies face critical membrane-related issues, especially in seawater environments, such as high ionic resistance, poor mechanical properties, and low selectivity towards chlorides. Here, we develop a reinforced composite membrane (RCM) featuring a chloride-blocking surface layer and PTFE support. The RCM exhibits low Cl^- permeability (1.03×10^{-6} cm^2 s^{-1}), over ten times lower than commercial membranes, while maintaining high hydroxide conductivity (118.03 mS cm^{-1}) and low swelling (3.52%). It delivers excellent performance in both anion exchange membrane water electrolysis (AEMWE) and asymmetrically fed seawater electrolysis (SWE), achieving 1.68 V at 1 A cm^{-2} (80 °C) in AEMWE and exceptional Cl^-/OH^- selectivity in SWE. Long-term operation tests show negligible performance degradation over 500 hours under both operation conditions. To the best of our knowledge, this is the first report of a membrane specifically engineered for asymmetrically fed SWE, addressing the critical challenges of chloride crossover and membrane deformation. Furthermore, the RCM's high dimensional stability and facile fabrication conditions enable scalable integration with functional nanomaterials (*e.g.*, NiFe-LDHs, rGO and Pt/C NPs), while minimizing the risk of nanoparticle detachment. This work establishes a versatile membrane design framework for advanced electrolysis systems and potential applications in related fields.

Introduction

Hydrogen, a clean energy carrier, has garnered significant attention for its superior energy storage and transportation capabilities.[1,2] With an energy density of up to 120 kJ per gram—three times that of gasoline—hydrogen stands out as a highly efficient energy source.[3] Its unique physicochemical properties enable efficient production, safe storage, and versatile applications, either as a direct fuel or for electricity generation through fuel cells.[4] Recent policy initiatives, such as the U.S. Inflation Reduction Act and the EU's Hydrogen Bank, have provided robust fiscal incentives and innovative financing mechanisms, accelerating the global expansion and strategic deployment of the hydrogen industry.[5] However, the current hydrogen production landscape remains heavily reliant on fossil fuels.[6,7] Although low-carbon alternatives like blue hydrogen, renewable natural gas from biomass, and methane pyrolysis have emerged, they face significant challenges, including biomass supply limitations, inadequate carbon capture infrastructure, methane leakage, and low CO_2 capture efficiency. Consequently, water electrolysis powered by renewable energy has emerged as a critical pathway to achieving net-zero emissions.[8]

Most low temperature electrolysis technologies, such as proton-exchange-membrane (PEM), require high-purity water, limiting their applicability in offshore and water-scarce regions. In contrast, seawater is readily available, and offshore wind energy is abundant, making seawater electrolysis (SWE) powered by renewable electricity a promising strategy for minimizing freshwater consumption and maximizing land use efficiency.[9,10] However, the complexity and variability of seawater composition pose significant challenges for SWE, particularly due to side reactions and electrode corrosion. Notably, seawater contains a high concentration (~0.5 M) of chloride (Cl^-) anions, which undergo chlorine evolution reactions (ClER, $Cl^- + 2OH^- \rightarrow ClO^- + H_2O + 2e^-$) at the anode, especially at high current densities.[11,12] With faster kinetics, ClER competes with the desired oxygen evolution reaction (OER), reducing OER efficiency and generating highly oxidative species such as chlorine and hypochlorite.[13,14] Worse still, the

---

[a] *Key Laboratory of Interfacial Physics and Technology, Shanghai Institute of Applied Physics, Chinese Academy of Sciences, Shanghai 201800, China. E-mail: wangtongshuai@sinap.ac.cn; zhanglinjuan@sinap.ac.cn*

[b] *University of Chinese Academy of Sciences, Beijing 10049, China*

strong binding affinity between Cl^- and active sites on electrocatalysts accelerates catalyst degradation, further shortening the electrolyzer's lifespan.[15] To address this issue, considerable efforts have been made to develop corrosion-resistant electrocatalysts with high OER selectivity.[16–18] While improvements in OER selectivity have been achieved, the corrosion of conductive substrates (*e.g.*, nickel) remains a significant challenge.[19,20]

To circumvent the potential range limitations, Strasser *et al.* proposed an alternative seawater electrolysis strategy based on an asymmetric electrolyte supply.[21] This approach employs an anion exchange membrane (AEM), Tokuyama A201, with a NiFe-layered double hydroxide (LDH) as the OER catalyst and commercial Pt/C as the hydrogen evolution reaction (HER) catalyst. Seawater is introduced exclusively into the cathode chamber, while the anode compartment is supplied with a chloride-free electrolyte. This strategy significantly reduces the ClER rate at the anode and achieves a high OER faradaic efficiency of over 94% along with relatively stable operation (~12 hours) at voltages above 1.7 V. Moreover, NiFe-LDH was identified as an effective and stable electrocatalyst in this environment. However, the authors mentioned that traces of Cl^- can still permeate through the commercial membrane into the anode chamber, inevitably accumulating over prolonged operation. Therefore, AEMs used in this novel electrolysis technology should possess high Cl^- rejection capability. At the same time, they should also exhibit sufficient mechanical strength and high OH^- conductivity to ensure long-term durability and minimize membrane resistance.

Despite the growing interest in asymmetric SWE, to date, no membrane has been specifically designed or modified to meet the stringent requirements of this application. For such systems, it is critical to simultaneously suppress Cl^- permeation, maintain low area-specific resistance, and ensure excellent dimensional stability under alkaline and ion-rich environments.[22,23] This challenge is further compounded by the fact that both Cl^- and OH^- are monovalent anions, making it even more difficult to achieve a high perm-selectivity.

Compared to traditional polymeric membranes, composite membranes combine two or more functional materials, leveraging the complementary advantages of each material to create synergistic effects.[24] This results in superior physicochemical properties, permeability, and selectivity. For example, reinforced membranes like Gore-Select® incorporate ion-exchange resins (*e.g.*, perfluorosulfonic acid resin) into high-strength porous fiber substrates, exhibiting significantly higher mechanical properties and dimensional stability than pure resin membranes. Lv *et al.* developed a QAPPT/Ni–Fe LDH hybrid membrane by incorporating NiFe-LDH with high OH^- conductivity into a polymer membrane,[25] this membrane demonstrated a high conductivity of 217.6 mS cm^{-1} at 80 °C, 1.6 times higher than that of pure polymer membranes.

Inspired by previous advances, we propose an innovative reinforced composite membrane (RCM) design for both SWE and AEMWE application. This membrane is based on a mechanically robust PTFE substrate infiltrated with ion-exchange resin. The use of PTFE allows the RCMs to be fabricated with reduced membrane thickness and lower ion-exchange resin loading, without compromising structural integrity. More importantly, the porous PTFE also serves as a filtration medium, allowing the facile deposition of various functional nanomaterials onto its surface *via* a simple vacuum filtration process. This results in a uniformly distributed, micron-thick functional layer. Our study shows that when NiFe-LDH is used as the building block of the functional layer, the resulting composite membrane can effectively suppress chloride ion crossover between the cathode and anode. Based on this design, we constructed an asymmetric SWE cell in which the cathode chamber is fed with alkaline simulated seawater and the anode with conventional alkaline electrolyte, achieving long-term and stable electrolysis performance. To the best of our knowledge, this is the first report to use such a membrane fabrication strategy to regulate interfacial chloride-blocking properties for asymmetric SWE cells, potentially offering a new alternative approach to direct seawater splitting. In addition, we found that the NiFe-LDH-based RCM also provides excellent electrolyte wettability and high OH^- transport capability, resulting in strong performance under standard AEMWE conditions. Finally, we explored the compatibility of this method with different nanomaterials, such as reduced graphene oxide (rGO) nanosheets and Pt/C nanoparticles, demonstrating that this fabrication strategy is highly adaptable to different functional layers and can be extended to a broader range of applications.

Experimental

Preparation of RCM membranes

The RCMs with a NiFe-LDH functional layer (denoted as RCM-LDH) were prepared as follows. NiFe-LDH powders (synthesized according to a previously reported method[26]) were dispersed in a mixed solvent of isopropanol (IPA, ≥99.8%, Adamas-beta Inc., Shanghai, China) and deionized water (Milli-Q, >18.25 MΩ cm). The suspension was sonicated for 1 hour to ensure homogeneous dispersion. Subsequently, the suspension was vacuum-filtered through a porous polytetrafluoroethylene (PTFE) membrane (Jinchun Environmental Protection Technology Co., Ltd, Changzhou, China). To improve the uniformity of LDH deposition on the PTFE substrate, a microporous polyethylene (PE) membrane (Asahi Kasei Corporation, Japan) was placed beneath the PTFE during filtration. The resulting LDH-coated PTFE membrane was dried in an oven at 60 °C for 30 minutes, after which the PE membrane was carefully removed. The dried PTFE-NiFe membrane was then placed on a flat PTFE plate preheated to 50 °C. A commercial alkaline ionomer solution (Sustainion® XA-9, 5 wt% in ethanol, Dioxide Materials, USA) was gently poured onto the membrane surface and evenly distributed. Sustainion® XA-9 was selected as the ionomer due to its superior hydrophilicity and good compatibility with alcohol-based solvents, which promote efficient wetting and uniform dispersion within the porous PTFE matrix. These properties are critical for achieving a defect-free and mechanically robust composite membrane structure. Although other commercial ionomers are available, XA-9 offers a favorable balance of ionic conductivity, film-forming ability, and chemical stability under alkaline conditions, making it a suitable choice for our membrane design. The membrane was subsequently dried under controlled temperature and humidity (50–70 °C) for 12 hours, yielding the final RCM-LDH sample.

RCM membranes incorporating other functional layers, including reduced graphene oxide (rGO) and Pt/C nanoparticles, were prepared using the same procedure, replacing the NiFe-LDH dispersion with the respective nanomaterial suspensions. The control RCM without any functional layer was fabricated by directly casting the 5 wt% ionomer solution onto the PTFE substrate and curing at 70 °C for 12 hours. Once the reinforced membrane was prepared, it was immersed in 1 M KOH solution at room temperature for 12 hours. After soaking, the membrane remained in a wet state without drying before electrochemical measurements.

Preparation of electrodes

Both the cathode and anode electrodes were fabricated using the catalyst-coated substrate (CCS) method. Catalyst inks were uniformly sprayed onto the respective substrates using an SCP102 ultrasonic spraying machine (Suzhou Sinero Technology Co., Ltd, China). For the anode, homemade NiFe-LDH powder was used as the catalyst, and commercial nickel felt (60% porosity, Zhejiang Changda, China) served as the substrate. The cathode was prepared using commercial PtNi catalyst (50 wt% Pt, Shanghai Jiping New Energy Technology Co., Ltd, China) deposited on TGP-H-060 carbon paper (Toray Industries, Inc., Japan). Notably, the NiFe-LDH catalyst used here was identical to that employed in the fabrication of the RCM membranes. The catalyst loading for both electrodes was 2.5 mg cm^{-2}, excluding the amount of LDH embedded in the functional layer of the membrane.

Material characterization

The surface morphology and cross-section of the synthesized RCM membranes was examined using field-emission scanning electron microscopy (FE-SEM) combined with energy dispersive X-ray spectroscopy (EDS) (Zeiss Crossbeam 540, Germany). In the present study, an accelerating voltage of 5 kV was applied for surface morphology and cross-sectional measurement, while 10 kV was applied for EDS measurement. Cross-sectional samples were prepared by carefully cutting membrane strips in liquid nitrogen. X-ray diffraction (XRD) analysis of the RCMs was conducted using a SmartLab X-ray diffractometer (Rigaku, Japan). The testing range is from 5° to 70°, with a scanning rate of 5° min^{-1}. The X-ray photoelectron spectroscopy (XPS) analysis of the RCM were carried out on a ESCALAB Xi+ XPS instrument (ThermoFisher Scientific, Czech Republic), with a monochromatized Al target X-ray source and an energy step size of 0.1 eV. The Ni and Fe L-edge soft X-ray absorption spectra of NiFe-LDHs within the modification layer of RCM-LDH were collected at the TLS 11A1 beamline of the Taiwan Light Source. The mechanical properties of RCMs were tested using a 3366 Universal Testing Machine (Instron, USA). The tensile test was conducted at a speed of 2 mm min^{-1} using rectangular specimens with a width of 10 mm and a gauge length (distance between clamps) of 20 mm. The hydrophilicity of the membrane surface was analyzed by conducting static water contact angle tests using a droplet shape analysis instrument (Kruss DSA30S, Germany), with a single addition of 5 microliters of deionized water. Light transmittance of membranes was tested using a visible light transmittance tester (Linshang LS160, Shenzhen Linshang Technology Co., Ltd, China). The in-plane ionic conductivity of the membrane was measured at various temperatures using a custom-built setup, employing two platinum wires as probes.

To test the swelling ratio (SR) and water uptake (WU), membrane samples were first dried at 60 °C overnight in vacuum oven and then immersed in aqueous KOH solutions (1 M) for 24 hours. The dimensions and weight of the dried and wet membrane were recorded. SR was calculated using the following relation:

$$\mathrm{SR} = \frac{L_{\mathrm{wet}} - L_{\mathrm{dry}}}{L_{\mathrm{dry}}} \times 100\% \tag{1}$$

where L_{wet} and L_{dry} represent the length of the wet and dried membrane samples, respectively.

WU was calculated with the following equation:

$$\mathrm{WU} = \frac{W_{\mathrm{w}} - W_{\mathrm{d}}}{W_{\mathrm{d}}} \times 100\% \tag{2}$$

where W_{w} and W_{d} represent the weights of the wet and dried membrane samples, respectively.

The chloride ion permeation test was carried out using a CH2010-S electrolyte/diffusion cell (Shanghai Ciyue, China). The open area of the samples was 1.77 cm^2 and the volume of each half cell was 50 mL. During the measurement, the membrane sample was sandwiched by two half-cell. One cell was filled with 2 M NaCl aqueous solution while the other was filled with DI water. The chloride permeation rate of membranes was determined by periodically recording the Cl$^-$ concentration in the receiving compartment using a chloride ion content analyzer (Kerui SSWY-810, Shaoxing Kerui Instrument Co., Ltd, China). The analyzer operates based on the ion-selective electrode method. Prior to each measurement, the electrode was calibrated using a series of NaCl standard solutions to ensure accurate and linear response. During the permeation test, samples were taken from the receiving side at regular intervals and measured immediately to minimize error. All measurements were performed at room temperature, and each data point represents the average of at least three independent tests.

The chloride permeation rate P was calculated using the following equation:

$$P = \frac{J \times L}{A \times \Delta C} \tag{3}$$

where J is the Cl$^-$ mol flux (mol s^{-1}), L is the membrane thickness (cm), A is the active area (cm^2), and ΔC is concentration gradient (mol cm^{-3}).

Electrolysis performance evaluation

All electrolysis tests were performed using the zero-gap flow cell with serpentine flow field. The active area of the electrode and membrane was 1 cm^2 for polarization measurements and 9 cm^2 for durability measurements. A smaller active area was chosen for polarization measurements due to the limited measurement range of the testing equipment, particularly at high current densities. All the polarization curves presented in this study are IR-included. Prior to testing, all samples were pretreated by immersing the dry membranes in 1 M KOH for 24 hours. During the AEMWE tests, 1 M KOH electrolyte solution was circulated through the cathode and anode compartments using a LABN1-III peristaltic pump (Innofluid Co., Ltd China) with a flow rate of 12 mL min^{-1}. During the asymmetric SWE test, a simulated seawater electrolyte consisted of 0.5 M KOH + 0.5 M NaCl was used as catholyte. The anolyte for SWE test contained 1 M KOH. The cell temperature was controlled using a STC101 thermocouple-heating element combination (Suzhou Sinero Technology Co., Ltd China). Before SWE polarization test, a 1-hour galvanostatic pre-conditioning step was conducted at 200 mA cm^{-2} to ensure stabilization of electrode–electrolyte interfaces and allow sufficient Cl^- migration toward the anode side, better simulating long-term operational conditions.

The polarization and durability tests of the assembled cell were conducted using a CE-4008Q-5V30A-SR 8-channel battery analyzer (Neware Technology Limited, China). Initially, the cell was stabilized by applying a low current density of 0.02 A cm^{-2} for 30 minutes. Subsequently, galvanostatic steady-state polarization curves were recorded by incrementally increasing the current density from 0.02 A cm^{-2} to 2 A cm^{-2} (SWE condition) and 4 A cm^{-2} (AEMWE condition) with a dwell time of 1 minute at each step. Durability was assessed under galvanostatic conditions, applying a current density of 1 A cm^{-2} for the 1 M KOH electrolyte and 0.2 A cm^{-2} for the simulated seawater electrolyte. Electrochemical impedance spectroscopy (EIS) analysis was employed as a diagnostic tool, using a SP-50e/150e, potentiostat (BioLogic, France). The EIS measurements were carried out in a frequency range of 100 kHz–0.1 Hz at 1.7 V, with a voltage amplitude of 20 mV. The impedance spectra were fitted to the corresponding equivalent circuit using the Zsim module (Bio-logic EC-lab) to obtain the electrochemical parameters of the MEA.

Results and discussion

Membrane fabrication and characterization

Fig. 1a illustrates the preparation process of the NiFe-LDH modified RCM membrane (RCM-LDH), which involves two major steps: (1) vacuum filtration of the NiFe-LDH suspension through a porous PTFE substrate, and (2) infiltration of the PTFE substrate and its interstitial spaces with the ion-exchange resin XA-9. Here, the PTFE substrate serves a dual function: acting as both a filtration medium and a mechanical support in the final membrane. Simultaneously, the ionomer not only promotes ion transport but also acts as an adhesive, ensuring strong integration between the surface layer and the substrate. NiFe-LDH was selected as the surface functional layer due to its well-documented advantages: it is a well-studied, non-precious metal catalyst with low cost, mature synthesis methods, and excellent stability in alkaline environments. Additionally, its strong hydrophilicity and catalytic activity may enhance the interfacial properties of the composite membrane and reduce interfacial resistance.[27] More importantly, NiFe-LDH is a highly effective Cl^- adsorbent, potentially acting as a screening layer to limit Cl^- permeation through the membrane.[28–30] This composite membrane design leverages the complementary strengths of each component, endowing the membrane with multiple functionalities. Nonetheless, this work primarily serves as a proof of concept. The material selection remains highly versatile: vacuum filtration is compatible with a wide range of candidate materials beyond NiFe-LDH, and both the substrate and ionomer can be flexibly tailored for specific applications.

The cross-sectional SEM images (Fig. 1b and e) reveal the internal architecture of the RCM-LDH membrane, comprising a reinforced layer approximately 8 μm thick and a surface modification layer of 2–3 μm thickness. In the modified surface layer, LDH nanoflowers are uniformly embedded within the reinforced matrix and tightly bonded *via* the ionomer. The top-view SEM image (Fig. 1c) further confirms that the slow vacuum filtration process enables a homogeneous deposition of NiFe-LDHs on the PTFE surface. On the membrane's backside, PTFE fibers are visibly intertwined with the ionomer (Fig. S1a and b), indicating effective infiltration—contrasted with the pristine PTFE morphology shown in Fig. S1c and d. A more intuitive indication of polymer infiltration is the change in membrane transmittance. Notably, embedding the ionomer into PTFE increased membrane transparency, raising transmittance from 8% to 21% (Fig. S2), which serves as an indicator of the ionomer infiltration into the substrate. The enhancement of transmittance is primarily due to the ionomer filling PTFE's micropores, as its refractive index closely matches that of PTFE.

Elemental mapping of Ni and Fe (Fig. 1f and g) *via* EDS confirms the uniform distribution of NiFe-LDHs throughout the RCM surface, with no evident aggregation, which is crucial for maintaining consistent electrochemical performance. The XRD pattern (Fig. 1h) reveals distinct diffraction peaks corresponding to both the PTFE substrate and the NiFe-LDH phase. The LDH-related peaks are in good agreement with the standard reference pattern (JCPDS No. 51-0463), indicating high crystallinity and phase purity of the deposited LDHs. Complementary Raman (Fig. 1i) spectroscopy further corroborates these findings.

The chemical composition of the RCM-LDH membrane was further characterized using XPS and total electron yield soft X-ray absorption spectroscopy (TEY-sXAS). The XPS survey spectrum of RCM-LDH (Fig. 2a) clearly displays the characteristic signals of Ni and Fe, confirming the successful incorporation of NiFe-LDHs into the RCM framework. High-resolution deconvolution of the Ni 2p region reveals two prominent peaks at 855.7 eV and 873.5 eV, corresponding to the Ni $2p_{3/2}$ and Ni $2p_{1/2}$ states of Ni^{2+}–OH, accompanied by two satellite features, which are indicative of the Ni^{2+} oxidation state in a hydroxide environment. The Fe $2p_{3/2}$ region can be deconvoluted into three components at 709.9 eV (Fe^{2+}), 712.0 eV (Fe^{3+}), and 713.9 eV (Ni LMM Auger peak), suggesting the coexistence of Fe in mixed oxidation states. To probe the surface electronic states

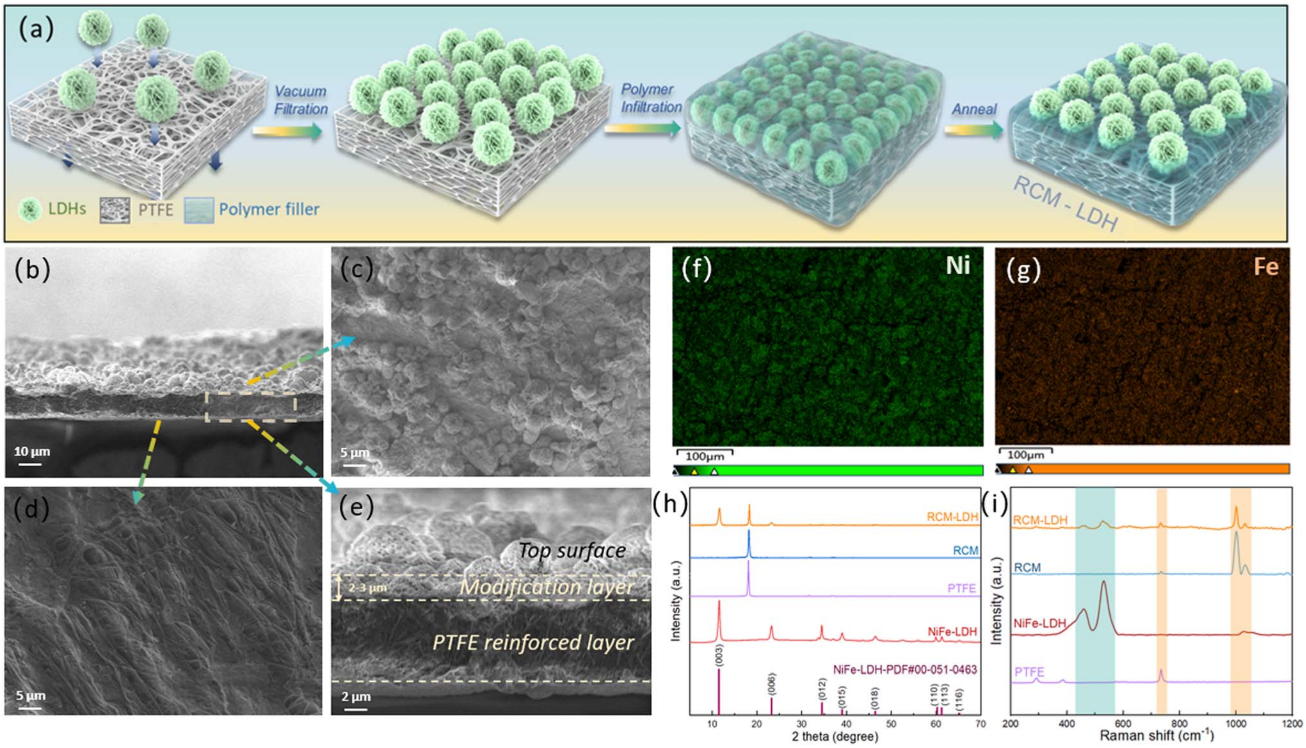

Fig. 1 (a) Schematic illustration of the RCM-LDH membrane preparation process. (b–e) SEM images of the RCM-LDH membrane: (b) cross-sectional view, (c) top view (modification layer), and (d) back-side view, (e) magnified cross-sectional view. (f–g) EDS elemental mapping of Ni (f) and Fe (g) composition on the RCM-LDH membrane top surface. (h) XRD patterns of the PTFE substrate, RCM (without LDH), RCM-LDH membrane, and NiFe-LDH catalyst. (i) Raman spectra of the PTFE substrate, RCM (without LDH), RCM-LDH membrane, and NiFe-LDH catalyst.

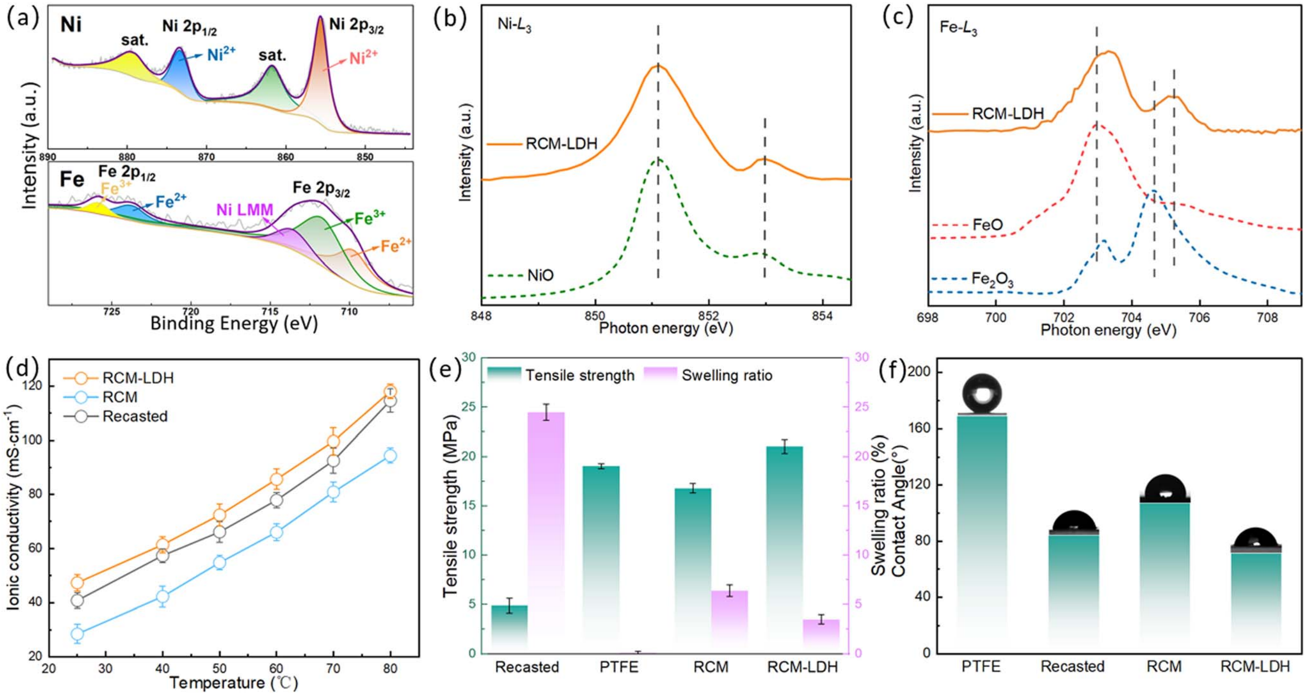

Fig. 2 (a) XPS spectra of Ni 2p and Fe 2p for RCM-LDH membrane. (b and c) sXAS spectra of the RCM-LDH: (b) Ni L3-edge and (c) Fe L3-edge. (d) Ionic conductivity of RCM (without LDH), RCM-LDH membrane, and non-reinforced recast membrane at different temperatures. (e) Tensile strength and swelling ratio of the PTFE substrate, RCM (without LDH), RCM-LDH membrane, and non-reinforced recast membrane. (f) Contact angles of the PTFE substrate, RCM (without LDH), RCM-LDH membrane, and non-reinforced recast XA-9 membrane.

of the NiFe-LDHs, TEY-sXAS was conducted at the Ni and Fe L_3-edges. As shown in Fig. 2b, the Ni L_3-edge spectrum of NiFe-LDHs closely matches that of NiO, a standard for Ni^{2+}, both in terms of multiplet features and energy position—indicating that Ni is in the +2 oxidation state. Likewise, the Fe L_3-edge spectrum aligns well with that of a Fe^{2+} reference (Fig. 2c), suggesting that Fe exists at least partially in the +2 oxidation state within the NiFe-LDHs.

Ionic conductivity is a critical parameter reflecting a membrane's ability to transport ions, directly influencing the energy loss associated with ion migration during water electrolysis. We evaluated the ionic conductivities of the RCM-LDH, RCM (without LDH), and recast membranes over a range of temperatures (Fig. 2d). Among them, the RCM without LDH exhibited the lowest conductivity across all tested temperatures. This is primarily attributed to the non-conductive nature of the PTFE substrate, which impedes ion transport within the membrane. In contrast, the incorporation of the LDH layer significantly improved ionic conductivity, even surpassing that of the conventional recast membrane. At 80 °C, the RCM-LDH achieved a maximum in-plane conductivity approaching 120 mS cm^{-1}. This enhancement can be attributed to two factors: (1) the LDH layer increases the membrane's wettability toward the electrolyte—particularly important given PTFE's inherently hydrophobic surface—and (2) LDHs themselves exhibit intrinsic ionic conductivity. Notably, the conductivity was measured using the in-plane method, where the contribution of the surface LDH layer is more pronounced. However, this may not fully reflect the through-plane ion transport direction typical in practical membrane operation. Therefore, for layered composite membranes, surface resistance or area-specific resistance (ASR) is often a more relevant and representative indicator of ion transport capability, as discussed later.

Tensile strength and swelling ratio are key indicators of the membrane's mechanical stability. High tensile strength and low swelling ratio are generally desirable, as they reduce the risk of mechanical failure or dimensional instability during cell assembly and prolonged operation. As shown in Fig. 2e, the PTFE substrate significantly enhances the mechanical robustness of the RCM series, yielding tensile strengths of 21 MPa—markedly higher than that of the non-reinforced recast membrane (4.9 MPa). Moreover, the reinforcement drastically lowers the swelling ratio from 24.5% (recast membrane) to 6.4% (RCM). The addition of the LDH surface layer further suppresses swelling, reducing the final swelling ratio to just 3.5%. Such low swelling behavior is advantageous in practical applications, as excessive swelling often leads to embrittlement, compromising mechanical durability and interfacial adhesion under electrolysis conditions.

Another important function of the surface LDH layer is to enhance wettability. As illustrated in Fig. 2f, the pristine PTFE substrate exhibits a high water contact angle of 169°, indicative of poor hydrophilicity. Upon ionomer infiltration (RCM without LDH), the contact angle decreases to 107°, yet still remains relatively high—typically, AEMs exhibit contact angles below 100°,[31,32] This suboptimal wettability hinders effective electrolyte contact. The introduction of the hydrophilic LDH layer significantly improves surface wettability. As the LDH content increases, the contact angle progressively decreases, reaching as low as 71°, demonstrating that the LDH surface coating effectively enhances hydrophilicity and promotes better electrolyte penetration.

Assessment for asymmetric SWE performance

To evaluate the electrochemical performance of RCM-LDH membranes in seawater electrolysis, we constructed an asymmetric electrolyzer configuration (Fig. 3a), wherein the catholyte consisted of 0.5 M NaCl + 0.5 M KOH to simulate alkaline seawater, the mixed electrolyte of 0.5 M KOH and 0.5 M NaCl was used without any pretreatment, while the anolyte was 1 M KOH. To mitigate cross-membrane water transport in the asymmetrically fed configuration, 1 M KOH was applied on the anode side, while a mixture of 0.5 M KOH and NaCl was used on the cathode side to better balance the osmotic pressure. This arrangement helps reduce the driving force for water migration caused by electrolyte concentration differences. During operation at 200 mA cm^{-2} for 72 hours (Fig. S10), the liquid levels in the anode and cathode storage tanks were monitored, revealing a slight increase in the cathode seawater volume and a corresponding decrease in the anode alkaline solution volume by approximately 4.6 mL per 500 mL. The calculated water flux across the membrane was approximately 0.16 L (m^{-2} h^{-1}), indicating a low rate of water transport. This water movement is primarily attributed to electro-osmotic drag and osmotic pressure effects, where water molecules and hydroxide ions migrate from the cathode side to the anode side. Prior to detailed performance testing, the chloride ion blocking capability of RCM-LDH was systematically investigated *via* a diffusion-based permeation test. A commercial membrane, Fumasep® FAA-3-20 (Fumasep BWT GmbH, Germany), with a comparable thickness (∼20 μm), was used as a reference. The chloride permeability was quantified by monitoring the temporal variation of Cl^- concentration in the receiving compartment (Fig. 3b). The RCM-LDH exhibited a Cl^- permeability of 0.71×10^{-5} kmol (m^{-2} s^{-1}), which is nearly one order of magnitude lower than that of the unmodified RCM (1.94×10^{-5} kmol (m^{-2} s^{-1})) and significantly lower than that of the commercial FAA-3-20 membrane (2.18×10^{-5} kmol (m^{-2} s^{-1})) (Fig. 3c). This enhancement in Cl^- rejection is attributed to the multivalent Ni and Fe sites in the LDHs, which strongly adsorb negatively charged Cl^- ions,[28] as well as the nanoflower-like morphology (Fig. 1c), which provides a high surface area for ion adsorption. It is important to note that, unlike in electrocatalytic applications—where Cl^- adsorption on NiFe-LDHs impairs catalytic performance—in the RCM-LDH membrane, the primary role of the LDH layer is to act as a physical and chemical barrier for Cl^- transport while simultaneously improving surface wettability.[29,30]

The polarization curves and impedance spectrum of SWE cells with different membranes were recorded at 60 °C, a typical temperature adopted in most research. The high-frequency resistance (HFR) obtained by fitting double CPEs equivalent circuit represents the overall ohmic resistance of the system, containing contributions from the membrane, electrodes,

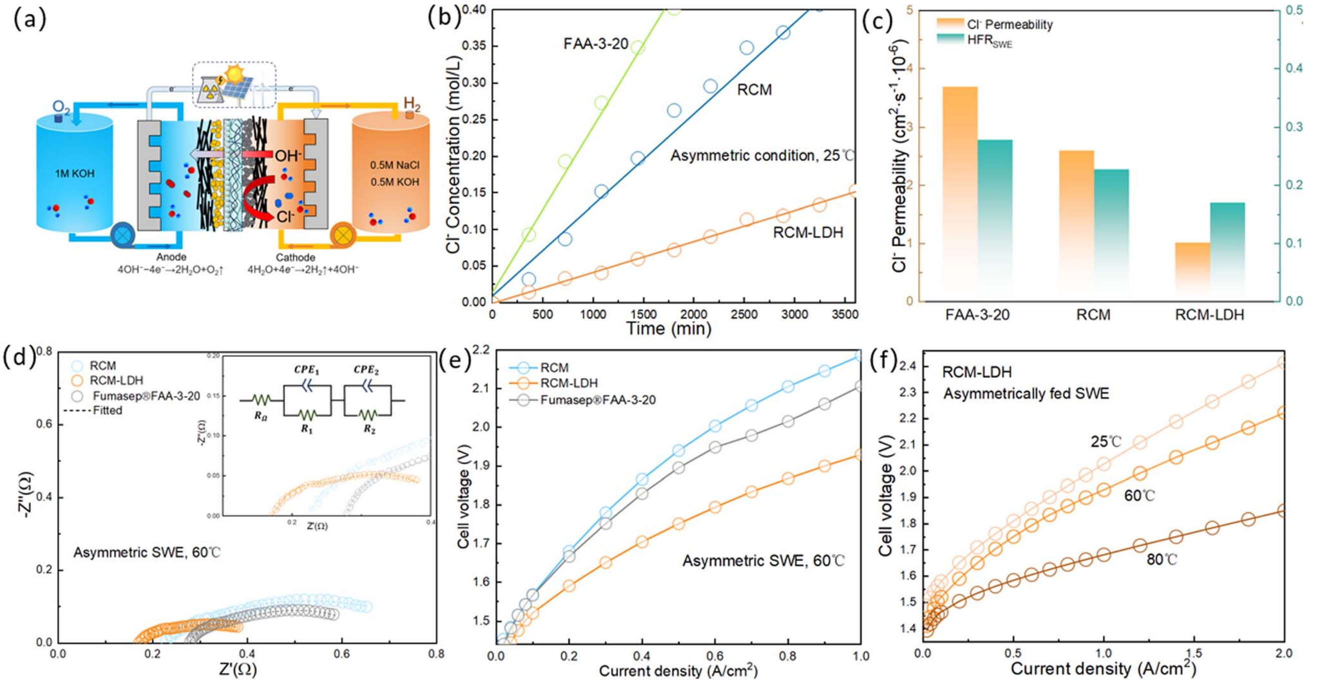

Fig. 3 (a) Schematic illustration of the asymmetrically fed SWE cell configuration. The catholyte consists of 0.5 M NaCl + 0.5 M KOH (simulated alkaline seawater), while the anolyte is 1 M KOH. The two compartments are separated by the membrane under investigation. (b) Cl^- permeation profiles of commercial Fumasep® FAA-3-20 membranes, RCM and RCM-LDH, showing the evolution of chloride concentration in the permeation compartment over time. (c) Corresponding Cl^- diffusion rate in the permeation test and high-frequency resistance (HFR) values for the three membranes. (d) Nyquist plots of electrolysis cells using RCM, RCM-LDH, and Fumasep® FAA-3-20 membranes, measured at 60 °C and 1.7 V. (e) Polarization curves of cells equipped with RCM, RCM-LDH, and Fumasep® FAA-3-20 membranes at 60 °C. (f) Polarization curves of cell equipped RCM-LDH operated at 25 °C, 60 °C, and 80 °C.

electrolyte, cell body, and external circuit. Since all experimental conditions except the membrane were identical, the observed variations in HFR primarily stem from differences in membrane properties.

As shown in Fig. 3c and d, the measured HFR for FAA-3-20 is the highest (0.279 Ω cm^2), followed by the unmodified RCM (0.228 Ω cm^2). The introduction of a NiFe-LDH modification layer significantly reduced HFR to 0.171 Ω cm^2 due to improved interfacial wettability. In addition to the ohmic resistance (HFR value), another key parameter influencing cell performance is the polarization resistance (R_{pol}), which primarily governs the polarization losses associated with the charge transfer process.[33] The polarization resistance (R_{pol}) also varied significantly among the membranes (Table S1). RCM-LDH achieved the lowest R_{pol} values of 0.260 Ω cm^2, in contrast to the much higher values observed for unmodified RCM (0.591 Ω cm^2) and FAA-3-20 (0.406 Ω cm^2), reflecting improved electrolyte wettability and reduced Cl^- crossover in the modified membranes. As illustrated in Fig. 3e, the polarization curves revealed that membranes with LDH layers exhibited the lowest cell voltages, correlating with their reduced ohmic losses and enhanced Cl^- barrier functionality. Cl^- crossover is known to facilitate the CIER at the anode, which elevates the anode potential and degrades performance.[34] At 1 A cm^{-2}, the RCM-LDH cell achieved a voltage of ~1.9 V, whereas the unmodified RCM reached ~2.2 V (Fig. 3f), clearly demonstrating the efficacy of the LDH coating in mitigating Cl^- migration.

Assessment for AEMWE performance

The electrochemical performance of the fabricated RCM membranes was further evaluated under conventional AEMWE configurations, as shown in Fig. 4a. In contrast to the previously discussed asymmetric SWE system, where membrane selectivity is critical, AEMWE places greater emphasis on minimizing membrane resistance. To finely adjust the membrane's ohmic resistance, we systematically tuned the surface loading of LDH from 0.1 to 0.9 mg cm^{-2}. The corresponding membranes were denoted as RCM-LDH-0.1, RCM-LDH-0.3, RCM-LDH-0.5, RCM-LDH-0.7, and RCM-LDH-0.9. Fig. 4b displays the impedance Nyquist plots of AEMWE single cells operated at 60 °C and 1.7 V. Fitting parameters obtained using a double-CPE equivalent circuit model are summarized in Table S1. The commercial Fumasep® FAA-3-20 membrane showed the highest HFR of 0.185 Ω cm^2, attributable to its relatively low ionic conductivity. The unmodified RCM membrane exhibited a slightly lower HFR of 0.170 Ω cm^2, likely due to the hydrophobic and non-conductive nature of the PTFE substrate. Upon incorporation of the LDH surface layer, the HFR values decreased significantly. Among all modified samples, RCM-LDH-0.5 achieved the lowest HFR of 0.127 Ω cm^2. However, further increasing the LDH loading led to a gradual rise in HFR (RCM-LDH-0.7: 0.132 Ω cm^2; RCM-LDH-0.9: 0.137 Ω cm^2), possibly due to the formation of a thicker interfacial layer that hindered OH^- transport and offset the benefits of enhanced hydrophilicity. It

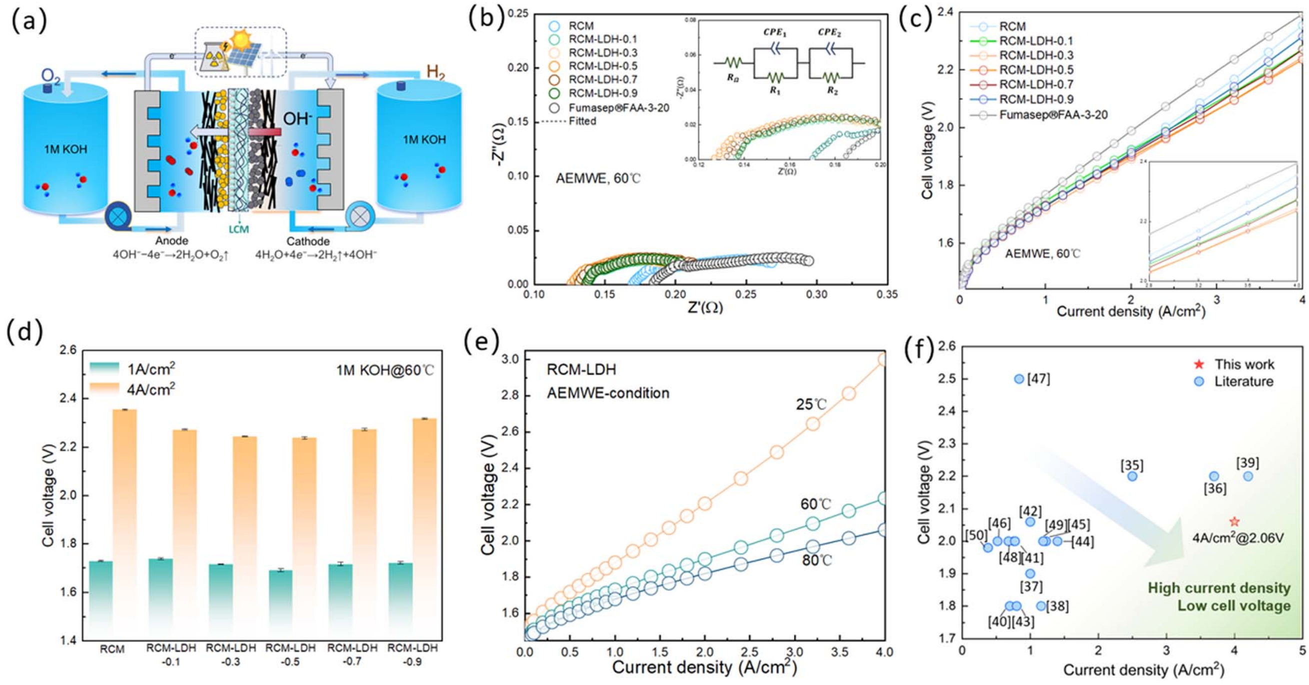

Fig. 4 (a) Schematic for AEMWE cell configuration (b–f) electrolysis performance of AEMWE cells assembled with different membranes, using 1 M KOH electrolyte at both the anode and cathode: (b) Nyquist plot at 60 °C and 1.7 V, (c) polarization curves at 60 °C; (d) cell voltage at 60 °C and current density of 1 A cm^{-2} and 4 A cm^{-2}, (e) polarization curves of the AEMWE cell assembled with RCM-LDH-0.5 membrane recorded at 25, 60, and 80 °C, respectively. (f) Comparison of operation voltage with reported works.[35–50]

is worth noting that all membranes showed higher HFR values under asymmetric SWE conditions than under AEMWE. For example, the HFR of RCM-LDH-0.5 increased from 0.127 Ω cm^2 in AEMWE to 0.171 Ω cm^2 in SWE, mainly due to the lower ionic strength of the seawater catholyte and the inherently lower mobility of Cl^- ions compared to OH^-.

With the incorporation of surface layer, R_{pol} significantly decreases from 0.18 Ω cm^2 ($R_1 = 0.024$ Ω cm^2, $R_2 = 0.156$ Ω cm^2) for the unmodified RCM to 0.08–0.09 Ω cm^2 for the RCM-0.1–0.9 membranes (Fig. 4b). The reduction in R_{pol} is likely due to presences of catalytic NiFe-LDHs on membrane–electrode interface, which provide additional active sites—although this was not the primary objective of our membrane design. Moreover, previous results already demonstrated that LDH surface layers enhance membrane hydrophilicity (Fig. 2d), thereby improving electrolyte wettability. This, in turn, may shorten the ion transport pathway between the membrane and the catalyst layer. Nevertheless, as shown in Table S1, R_{pol} remains largely unchanged with increasing LDH content, possibly because only the exposed LDH layer at the surface contributes to reducing R_{pol}.

The polarization behaviors of AEMWE cells equipped with the RCM-LDHs and Fumasep® FAA-3-20 are compared in Fig. 4c. The polarization curves were recorded at an elevated temperature of 60 °C. Compared to the commercial FAA-3-20, which has a higher resistance, the RCM-LDH membranes exhibited significantly lower cell voltages. Among them, RCM-LDH-0.5 demonstrated the best water electrolysis performance. At a current density of 1 A cm^{-2}—a value of particular interest to industry—RCM-LDH-0.5 exhibited the lowest cell voltage of 1.68 V, primarily attributed to its minimal membrane resistance, as confirmed by impedance measurements. The superior performance of RCM became even more pronounced at higher current densities. At 4 A cm^{-2}, the cell voltage for FAA-3-20 reached 2.42 V, which was 210 mV higher than that of RCM-LDH-0.5 (2.21 V). To further assess its electrolysis performance, the polarization curve of the electrolyzer with RCM-LDH-0.5 was recorded at various operating temperatures (Fig. 4e). As the temperature increased, the AEMWE performance of RCM-LDH-0.5 improved accordingly. At 80 °C, the RCM-LDH-0.5 membrane achieved a lower cell voltage of 1.65 V and 2.05 V at current densities of 1 A cm^{-2} and 4 A cm^{-2}, respectively. This enhancement is attributed to improved electrode reaction kinetics, as well as enhanced electron, ion, and mass transport. Notably, the thermodynamic potential of the water-splitting reaction decreases by ~8.5 mV per 10 °C.[51] The 25 °C curve shows a slight deviation from the general trend at high current densities, which might be attributed to increased mass transport resistance or interfacial impedance under low-temperature conditions. Moreover, at 25 °C, gas removal from diffusion layers becomes less efficient due to reduced diffusivity. These factors can lead to gas accumulation and localized flooding, which in turn increase the parasitic impedance.

Long-term stability evaluation

To assess long-term stability, electrolyzers with the best-performing RCM-LDH-0.5 membrane underwent 500-hour galvanostatic operation at 1.0 A cm^{-2} for AEMWE and 200 mA cm^{-2} for asymmetric SWE (Fig. 5a). Previous tests confirmed

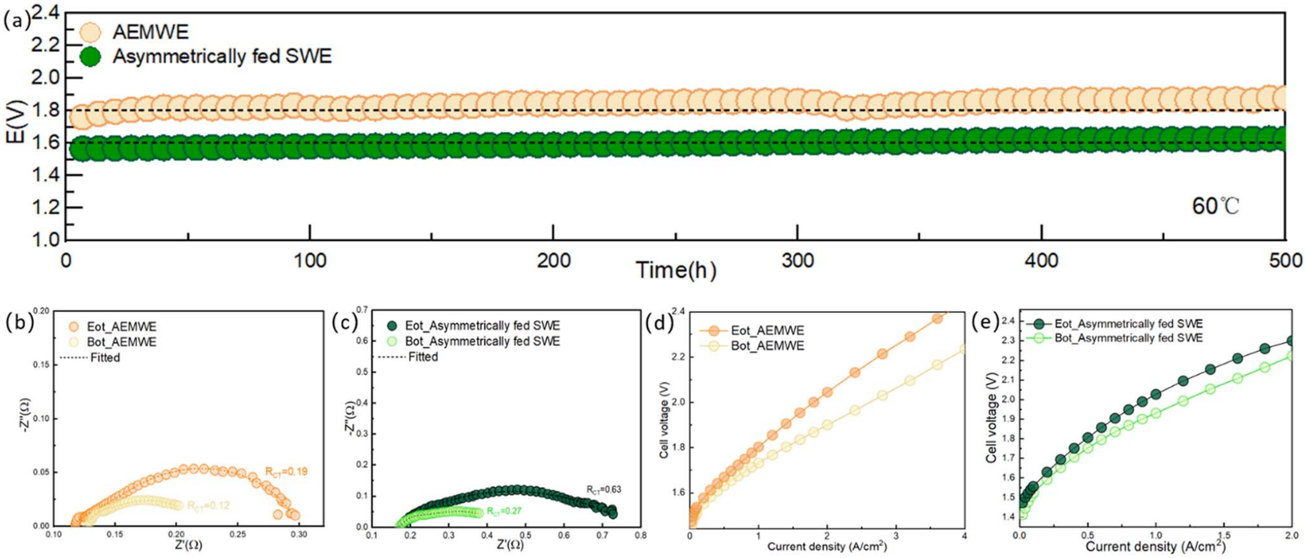

Fig. 5 (a) Cell voltage recorded during 500-hour galvanostatic operation for AEMWE and asymmetric SWE single-cell assembled with RCM-LDH-0.5 membrane, (b) beginning-of-test (Bot) and end-of-test (Eot) Nyquist plot of the AEMWE cell, (c) Bot and Eot Nyquist plot of the asymmetric SWE cell. (d) Bot and Eot polarization curves of the AEMWE cell. (e) Bot and Eot polarization curves of asymmetric SWE cell.

that the membrane can block part of the chloride ions, but some chloride crossover still occurs over time. At high current densities, this crossover increases, leading to possible chlorine-related side reactions. Additionally, the asymmetric-fed SWE system inherently shows lower electrolysis performance than AEMWE, and higher current densities cause significantly increased cell voltage. Therefore, long-term durability tests for the asymmetric-fed SWE were performed at 200 mA cm^{-2} to balance performance and stability.

Our results demonstrate that the membrane maintained excellent stability in both environments. In SWE stability test, the cell voltage gradually increased from 1.56 V at the start to 1.65 V after 500 hours, exhibiting remarkable stability and effectively blocking chloride ions. In contrast, the commercial FAA-3-20 membrane showed a rapid voltage and electrode corrosion increase after 48 hours.

Under AEMWE conditions, the voltage increased from 1.71 V to 1.82 V in the first 100 hours, likely due to catalyst detachment. However, degradation slowed over the next 400 hours, with the voltage rising gradually to 1.88 V. Impedance spectra before and after the stability tests under both conditions indicate that the HFR remained largely unchanged (Fig. 5b and c), suggesting minimal membrane resistance variation. The more significant change was observed in the R_{ct}. Specifically, R_{ct}. in AEMWE and SWE increased from 0.12 and 0.27 Ω cm^2 before the test to 0.19 and 0.63 Ω cm^2 after the test, indicating that catalyst deactivation or detachment was the primary cause of performance degradation. Corresponding polarization curves before and after the 500-hour test (Fig. 5d and e) showed a moderate increase in voltage, indicating some performance degradation but retaining overall electrochemical activity. SEM images of the electrodes before and after the 500-hour durability test (Fig. S11–S14) showed minor catalyst detachment, while the overall electrode structure remained largely intact.

Broader applicability of the proposed method

A key advantage of the proposed membrane fabrication method in this work lies in its simplicity and broad applicability. The modification layer can be introduced through a facile vacuum filtration process, and the porous substrate used for filtration does not need to be removed, serving directly as the structural support of the reinforced membrane.

To demonstrate the versatility of this approach, we fabricated two additional types of modified RCMs using the same protocol: one incorporating Pt/C nanoparticles, a commonly used cathode catalyst, and another using reduced graphene oxide (rGO) nanosheets, which are catalytically inert but possess a two-dimensional sheet structure. Cross-sectional SEM images of these membranes (Fig. 6a and b) confirm the successful formation of well-defined surface layers, suggesting that this method can be extended to a wide range of material systems. We further evaluated the Cl$^-$ permeation behavior of these membranes. As shown in Fig. 6c and d, the rGO-modified membrane (RCM-rGO) exhibited the lowest Cl$^-$ permeability, approximately one-third that of RCM-LDH, highlighting the excellent barrier properties of the rGO-based surface layer. In contrast, the Pt/C-modified membrane (RCM-Pt/C) showed comparatively poor Cl$^-$ rejection. As shown in Fig. 6e and f, EIS results indicate that RCM-rGO exhibits higher HFR than RCM-LDH and RCM-Pt/C, likely due to reduced OH$^-$ transport through the rGO interlayer. RCM-Pt/C demonstrates lower resistance but weaker Cl$^-$ selectivity and higher material cost. In comparison, RCM-LDH offers a more balanced performance in terms of conductivity and selectivity.

These examples are primarily intended to demonstrate the generalizability of our 'surface engineering + reinforcement' strategy. With further exploration, we anticipate that this approach can be applied to a broader range of functional

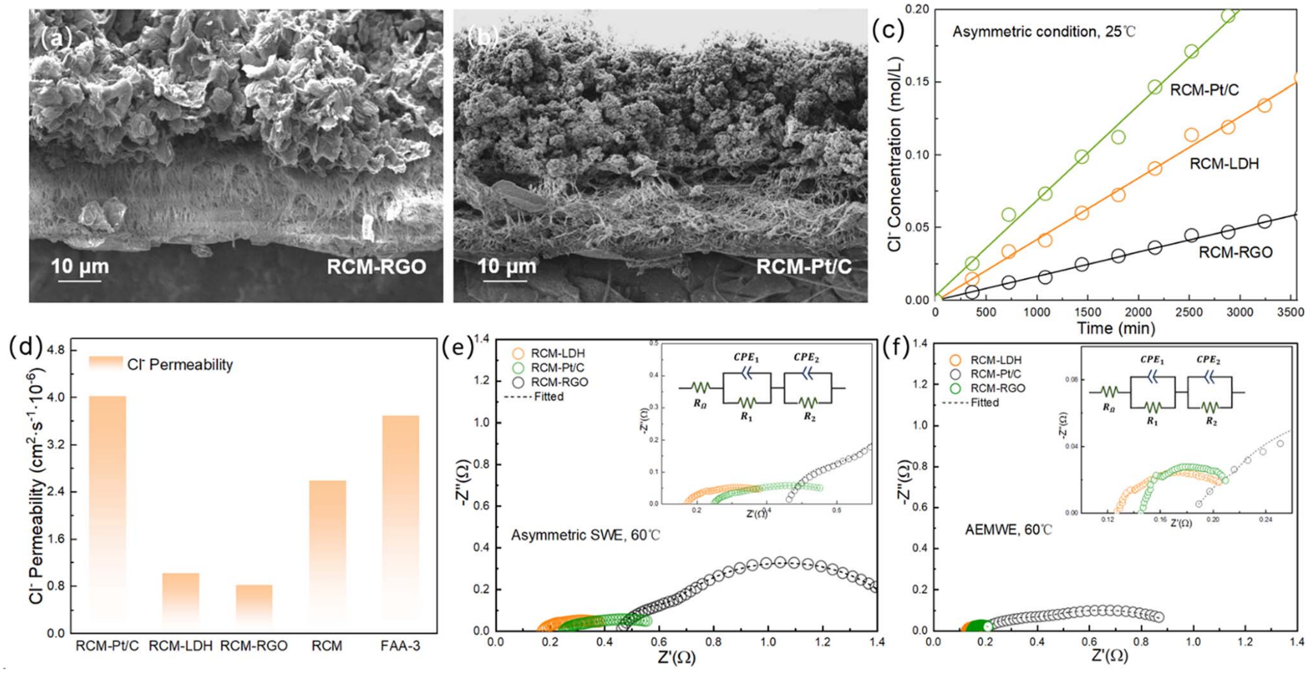

Fig. 6 (a and b) Cross-sectional SEM image of RCMs modified with (a) reduced graphene-oxide (rGO) nanosheets (RCM-rGO) and (b) platinum/carbon (Pt/C) nanoparticles (RCM-Pt/C). (c) Time-dependent chloride-ion permeation curves for RCM-LDH, RCM-rGO, and RCM-Pt/C, showing the evolution of Cl^- concentration in the permeate compartment. (d) Comparison of Cl^- permeability, high-frequency resistance under SWE conditions (HFR_{SWE}) and under conventional AEMWE conditions (HFR_{AEMWE}) for the three membranes. (e) Nyquist plots of asymmetric SWE cells employing the three membranes, recorded at 60 °C and 1.7 V (f) Nyquist plots of AEMWE cells employing the three membranes, recorded at 60 °C and 1.7 V.

materials tailored for specific separation and electrochemical performance requirements.

Conclusions

This study introduces an innovative layered composite membrane (RCM) design that effectively tackles key challenges in seawater electrolysis for hydrogen production. By incorporating a NiFe-LDH-based Cl^- blocking layer and a porous PTFE support, the RCM achieves an optimal balance of ion selectivity, low resistance, and mechanical durability, making it well-suited for both asymmetrically fed SWE and AEMWE. In AEMWE, the RCMLDH-0.5 membrane exhibited outstanding performance, maintaining a cell voltage of 1.68 V at 1 A cm^{-2}. In SWE, it effectively suppressed Cl^- migration, enabling stable operation with non-precious metal catalysts. Long-term durability tests further confirmed its stability, with minimal performance degradation over 500 hours under both conditions. These findings underscore the RCM's potential to advance hydrogen production, particularly in resource-limited regions. Importantly, the membrane fabrication strategy demonstrated in this work can be readily extended to other functional materials. By simultaneously enhancing mechanical robustness and ion selectivity, this approach offers a versatile platform to address persistent challenges such as membrane degradation and electrolyte crossover—not only in electrolyzers, but also in fuel cells and flow batteries. The universal design principles underlying this RCM architecture thus hold broad potential for advancing next-generation sustainable energy technologies.

Author contributions

Yuhui Gong: formal analysis, writing – review & editing, writing – original draft, data curation. Yuanman Ni: formal analysis, data curation, validation. Tian Lan: formal analysis, investigation. Han Song: formal analysis, investigation. Hao Zhang: writing – review, validation, investigation. Shujuan Wang: writing – review, investigation. Miaomiao Liu: writing – review, investigation. Tongshuai Wang: writing – review & editing, project administration, conceptualization, funding acquisition, validation, supervision. Jian-Qiang Wang: supervision, project administration, funding acquisition. Linjuan Zhang: supervision, project administration, funding acquisition.

Conflicts of interest

There are no conflicts to declare.

Data availability

Supporting data for this article, including SEM images, optical microscopy, EDS analyses, FTIR spectra, electrochemical characterization results, stability data, and a table summarizing EIS fitting parameters, are available at https://doi.org/10.1039/d5ta05372b.

Acknowledgements

This work was financially supported by Strategic Priority Research Program of the Chinese Academy of Sciences (Grant No. XDA0400000), National Science Foundation of China (Grant No. 22409205 and 22179141), Talent Plan of Shanghai Branch, Chinese Academy of Sciences (CASSHB-QNPD-2023-006), Young Talent Recruitment Program of Shanghai Institute of Applied Physics, CAS (Grant No. E3552401), the Photon Science Center for Carbon Neutrality, and Pujiang Talents Program (Grant No. 24PJA157).

Notes and references

1 M. Liu, Z. Yao, J. Gu, C. Li, X. Huang, L. Zhang, Z. Huang and M. Fan, Issues and opportunities facing hydrolytic hydrogen production materials, *Chem. Eng. J.*, 2023, **461**, 141918.

2 H. Kojima, K. Nagasawa, N. Todoroki, Y. Ito, T. Matsui and R. Nakajima, Influence of renewable energy power fluctuations on water electrolysis for green hydrogen production, *Int. J. Hydrogen Energy*, 2023, **48**(12), 4572–4593.

3 S. Cheng, X. Cheng, M. H. Tahir, Z. Wang and J. Zhang, Synthesis of rice husk activated carbon by fermentation osmotic activation method for hydrogen storage at room temperature, *Int. J. Hydrogen Energy*, 2024, **62**, 443–450.

4 K. Naseem, F. Qin, F. Khalid, G. Suo, T. Zahra, Z. Chen and Z. Javed, Essential parts of hydrogen economy: Hydrogen production, storage, transportation and application, *Renewable Sustainable Energy Rev.*, 2025, **210**, 115196.

5 A. Hoogsteyn, J. Meus, K. Bruninx and E. Delarue, Interactions and distortions of different support policies for green hydrogen, *Energy Econ.*, 2025, **141**, 108042.

6 C. Zhang, P. Qu, M. Zhou, L. Qian, T. Bai, J. Jin and B. Xin, Ionic Liquids as Promisingly Multi-Functional Participants for Electrocatalyst of Water Splitting: A Review, *Molecules*, 2023, **28**(7), 3051.

7 C. Feng, B. Xin, H. Li, Z. Jia, X. Zhang and B. Geng, Agaric-like cobalt diselenide supported by carbon nanofiber as an efficient catalyst for hydrogen evolution reaction, *J. Colloid Interface Sci.*, 2022, **610**, 854–862.

8 D. Tonelli, L. Rosa, P. Gabrielli, K. Caldeira, A. Parente and F. Contino, Global land and water limits to electrolytic hydrogen production using wind and solar resources, *Nat. Commun.*, 2023, **14**(1), 5532.

9 B. E. Logan, L. Shi and R. Rossi, Enabling the use of seawater for hydrogen gas production in water electrolyzers, *Joule*, 2021, **5**(4), 760–762.

10 A. Gaur, E. Enkhbayar, J. Sharma, S. Mhin and H. Han, Chloride-Ion Blocking in Seawater Electrolysis: Narrating the Tale of Likes and Dislikes Between Anode and Ions, *Energy Environ. Mater.*, 2025, **8**(1), e12817.

11 H. Xie, Z. Zhao, T. Liu, Y. Wu, C. Lan, W. Jiang, L. Zhu, Y. Wang, D. Yang and Z. Shao, A membrane-based seawater electrolyser for hydrogen generation, *Nature*, 2022, **612**(7941), 673–678.

12 T. Li, B. Wang, Y. Cao, Z. Liu, S. Wang, Q. Zhang, J. Sun and G. Zhou, Energy-saving hydrogen production by seawater electrolysis coupling tip-enhanced electric field promoted electrocatalytic sulfion oxidation, *Nat. Commun.*, 2024, **15**(1), 6173.

13 C. Huang, Z. Wang, S. Cheng, Y. Liu, B. Deng, S. Xu, L. Yu and Y. Yu, Challenges and strategies of chlorine inhibition in anode systems for seawater electrolysis, *Sci. China: Chem.*, 2024, **67**(10), 3198–3208.

14 P. Guo, D. Liu and R. Wu, Recent Progress in Design Strategy of Anode for Seawater Electrolysis, *Small Struct.*, 2023, **4**(12), 2300192.

15 X. Kang, F. Yang, Z. Zhang, H. Liu, S. Ge, S. Hu, S. Li, Y. Luo, Q. Yu, Z. Liu, Q. Wang, W. Ren, C. Sun, H.-M. Cheng and B. Liu, A corrosion-resistant RuMoNi catalyst for efficient and long-lasting seawater oxidation and anion exchange membrane electrolyzer, *Nat. Commun.*, 2023, **14**(1), 3607.

16 J. Li, Y. Liu, H. Chen, Z. Zhang and X. Zou, Design of a Multilayered Oxygen-Evolution Electrode with High Catalytic Activity and Corrosion Resistance for Saline Water Splitting, *Adv. Funct. Mater.*, 2021, **31**(27), 2101820.

17 W. Chen, W. Wei, F. Li, Y. Wang, M. Liu, S. Dong, J. Cui, Y. Zhang, R. Wang, K. Ostrikov and S.-Q. Zang, Tunable Built-In Electric Field in Ru Nanoclusters-Based Electrocatalyst Boosts Water Splitting and Simulated Seawater Electrolysis, *Adv. Funct. Mater.*, 2024, **34**(7), 2310690.

18 R. Fan, C. Liu, Z. Li, H. Huang, J. Feng, Z. Li and Z. Zou, Ultrastable electrocatalytic seawater splitting at ampere-level current density, *Nat. Sustainability*, 2024, **7**(2), 158–167.

19 S. Zhang, W. Xu, H. Chen, Q. Yang, H. Liu, S. Bao, Z. Tian, E. Slavcheva and Z. Lu, Progress in Anode Stability Improvement for Seawater Electrolysis to Produce Hydrogen, *Adv. Mater.*, 2024, **36**(37), 2311322.

20 D. Liu, Y. Cai, X. Wang, Y. Zhuo, X. Sui, H. Pan and Z. Wang, Innovations in electrocatalysts, hybrid anodic oxidation, and electrolyzers for enhanced direct seawater electrolysis, *Energy Environ. Sci.*, 2024, **17**(19), 6897–6942.

21 S. Dresp, T. Ngo Thanh, M. Klingenhof, S. Brückner, P. Hauke and P. Strasser, Efficient direct seawater electrolysers using selective alkaline NiFe-LDH as OER catalyst in asymmetric electrolyte feeds, *Energy Environ. Sci.*, 2020, **13**(6), 1725–1729.

22 H. B. Park, J. Kamcev, L. M. Robeson, M. Elimelech and B. D. Freeman, Maximizing the right stuff: The trade-off between membrane permeability and selectivity, *Science*, 2017, **356**(6343), eaab0530.

23 Q. Dai, Z. Liu, L. Huang, C. Wang, Y. Zhao, Q. Fu, A. Zheng, H. Zhang and X. Li, Thin-film composite membrane breaking the trade-off between conductivity and selectivity for a flow battery, *Nat. Commun.*, 2020, **11**(1), 1.

24 R. Vinodh, S. S. Kalanur, S. K. Natarajan and B. G. Pollet, Recent Advancements of Polymeric Membranes in Anion Exchange Membrane Water Electrolyzer (AEMWE): A Critical Review, *Polymers*, 2023, **15**(9), 2144.

25 B. Lv, Y. Yang, C. Yang, Z. Huang, Y. Zhou, W. Song, J. Hao and Z. Shao, Layered double hydroxide composite membrane for advanced alkaline water electrolysis, *Int. J. Energy Res.*, 2022, **46**(9), 11892–11902.

26 H. Zhong, T. Liu, S. Zhang, D. Li, P. Tang, N. Alonso-Vante and Y. Feng, Template-free synthesis of three-dimensional NiFe-LDH hollow microsphere with enhanced OER performance in alkaline media, *J. Energy Chem.*, 2019, **33**, 130–137.

27 X.-J. Zhai, Q.-X. Lv, J.-Y. Xie, Y.-X. Zhang, Y.-M. Chai and B. Dong, Advances in the design of highly stable NiFe-LDH electrocatalysts for oxygen evolution in seawater, *Chem. Eng. J.*, 2024, **496**, 153187.

28 P. Zhai, M. Xia, Y. Wu, G. Zhang, J. Gao, B. Zhang, S. Cao, Y. Zhang, Z. Li, Z. Fan, C. Wang, X. Zhang, J. T. Miller, L. Sun and J. Hou, Engineering single-atomic ruthenium catalytic sites on defective nickel-iron layered double hydroxide for overall water splitting, *Nat. Commun.*, 2021, **12**(1), 4587.

29 A. R. Jadhav, A. Kumar, J. Lee, T. Yang, S. Na, J. Lee, Y. Luo, X. Liu, Y. Hwang, Y. Liu and H. Lee, Stable complete seawater electrolysis by using interfacial chloride ion blocking layer on catalyst surface, *J. Mater. Chem. A*, 2020, **8**(46), 24501–24514.

30 E. Enkhtuvshin, S. Yeo, H. Choi, K. M. Kim, B.-S. An, S. Biswas, Y. Lee, A. K. Nayak, J. U. Jang, K.-H. Na, W.-Y. Choi, G. Ali, K. H. Chae, M. Akbar, K. Y. Chung, K. Yoo, Y.-C. Chung, T. H. Shin, H. Kim, C.-Y. Chung and H. Han, Surface Reconstruction of Ni–Fe Layered Double Hydroxide Inducing Chloride Ion Blocking Materials for Outstanding Overall Seawater Splitting, *Adv. Funct. Mater.*, 2023, **33**(22), 2214069.

31 C. Li, G. Wang, D. Yu, F. Sheng, M. A. Shehzad, T. He, T. Xu, X. Ren, M. Cao, B. Wu and L. Ge, Cross-linked anion exchange membranes with hydrophobic side-chains for anion separation, *J. Membr. Sci.*, 2019, **581**, 150–157.

32 J. Liao, X. Yu, Q. Chen, X. Gao, H. Ruan, J. Shen and C. Gao, Monovalent anion selective anion-exchange membranes with imidazolium salt-terminated side-chains: Investigating the effect of hydrophobic alkyl spacer length, *J. Membr. Sci.*, 2020, **599**, 117818.

33 M. Ranz, B. Grabner, B. Schweighofer, H. Wegleiter and A. Trattner, Dynamics of anion exchange membrane electrolysis: Unravelling loss mechanisms with electrochemical impedance spectroscopy, reference electrodes and distribution of relaxation times, *J. Power Sources*, 2024, **605**, 234455.

34 Z. Yu and L. Liu, Recent Advances in Hybrid Seawater Electrolysis for Hydrogen Production, *Adv. Mater.*, 2024, **36**(13), 2308647.

35 W. Ma, L. Tian, Q. Zhu, S. Zhang, F. Wang and H. Zhu, Highly Hydrophilic Zirconia Composite Anion Exchange Membrane for Water Electrolysis and Fuel Cells, *ACS Appl. Mater. Interfaces*, 2024, **16**(9), 11849–11859.

36 C. Simari, A. Caprì, M. H. Ur Rehman, A. Enotiadis, I. Gatto, V. Baglio and I. Nicotera, Composite anion exchange membranes based on polysulfone and silica nanoscale ionic materials for water electrolyzers, *Electrochim. Acta*, 2023, **462**, 142788.

37 N. Carboni, L. Mazzapioda, A. Caprì, I. Gatto, A. Carbone, V. Baglio and M. A. Navarra, Composite anion exchange membranes based on graphene oxide for water electrolyzer applications, *Electrochim. Acta*, 2024, **486**, 144090.

38 J. Choi, H. Kim, S. Jeon, M. G. Shin, J. Y. Seo, Y.-I. Park, H. Park, A. S. Lee, C. Lee, M. Kim, H.-S. Cho and J.-H. Lee, Thin Film Composite Membranes as a New Category of Alkaline Water Electrolysis Membranes, *Small*, 2023, **19**(37), 2300825.

39 C. Simari, M. H. Ur Rehman, A. Caprì, I. Gatto, V. Baglio and I. Nicotera, High-performance anion exchange membrane water electrolysis by polysulfone grafted with tetramethyl ammonium functionalities, *Mater. Today Sustainability*, 2023, **210**, 100297.

40 J. Choi, K. Min, Y.-H. Mo, S.-B. Han and T.-H. Kim, Understanding the Effect of Triazole on Crosslinked PPO–SEBS-Based Anion Exchange Membranes for Water Electrolysis, *Polymers*, 2023, **15**(7), 1736.

41 Y. Chen, Z. Yu, J. Tang, X. Zhang, S. Guo, X. Tang, Z. Chen and Y. Zhan, Functionalized MXene acts as a crosslinking agent to construct new anion exchange membranes for anion exchange membrane water electrolysis, *J. Power Sources*, 2025, **641**, 236875.

42 R. Gentile, S. C. Zignani, M. Zatoń, M. Dupont, F. Lecœur, N. Donzel, A. Amel, E. Tal-Gutelmacher, A. Salanitro, A. S. Aricó, S. Cavaliere, D. J. Jones and J. Rozière, Polybenzimidazole-Reinforced Terphenylene Anion Exchange Water Electrolysis Membranes, *ChemSusChem*, 2024, **17**(23), e202400825.

43 W. Zou, K. Peng, R. Ling, Q. Li, Y. Liu, T. Xu and Z. Yang, Robust and ultrathin pore-filling anion exchange membranes for water electrolysis, *AICHE J.*, 2025, **71**(6), e18769.

44 T. Yang, S. Huang, J. Wang, H. He, J. Xu, G. Hu, J. Zhou, H. Liang and C. Zhao, Durable cross-linked poly(carbazole)-based anion exchange membranes for alkaline water electrolysis, *Polymer*, 2025, **323**, 128195.

45 P.-S. Jhu, C.-W. Chang, C.-C. Cheng, Y.-C. Ting, T.-Y. Lin, F.-Y. Yen, P.-W. Chen and S.-Y. Lu, Non-precious high entropy alloys and highly alkali-resistant composite membranes based high performance anion exchange membrane water electrolyzers, *Nano Energy*, 2024, **126**, 109703.

46 Z. Xu, S. Delgado, V. Atanasov, T. Morawietz, A. S. Gago and K. A. Friedrich, Novel Pyrrolidinium-Functionalized Styrene-b-ethylene-b-butylene-b-styrene Copolymer Based Anion Exchange Membrane with Flexible Spacers for Water Electrolysis, *Membranes*, 2023, **13**(3), 328.

47 Y. Wang, T. Ban, M. Guo and X. Zhu, Poly(fluorenyl-indolinedione) based hydroxide conducting membrane for anion exchange membrane water electrolyzers, *Int. J. Hydrogen Energy*, 2024, **49**, 1123–1133.

48 Z. Xu, V. Wilke, J. J. Chmielarz, M. Tobias, V. Atanasov, A. S. Gago and K. A. Friedrich, Novel piperidinium-functionalized crosslinked anion exchange membrane with flexible spacers for water electrolysis, *J. Membr. Sci.*, 2023, **670**, 121302.

49 J. E. Kim, Y. H. Yun, H. Park, J. Albers, G. Doo, S. Lee, J. Seo, C. Lee, M. Kim, H.-S. Cho, S.-K. Kim, J. H. Lee, Y.-W. Choi

and J. H. Kim, Hydrogen-bonded QSEBS/ZrO2 mixed matrix anion exchange membranes for water electrolyzer, *Fuel*, 2024, **376**, 132684.

50 R. E. Coppola, D. Herranz, R. Escudero-Cid, N. Ming, N. B. D'Accorso, P. Ocón and G. C. Abuin, Polybenzimidazole-crosslinked-poly(vinyl benzyl chloride) as anion exchange membrane for alkaline electrolyzers, *Renewable Energy*, 2020, **157**, 71–82.

51 A. Lim, H.-j. Kim, D. Henkensmeier, S. Jong Yoo, J. Young Kim, S. Young Lee, Y.-E. Sung, J. H. Jang and H. S. Park, A study on electrode fabrication and operation variables affecting the performance of anion exchange membrane water electrolysis, *J. Ind. Eng. Chem.*, 2019, **76**, 410–418.